Interpretation®

Contributions of the Horizontal OBN Components to P-wave Imaging

Journal:	*Interpretation*
Manuscript ID	INT-2024-0145.R1
Manuscript Type:	2024-04 Geological and geophysical interpretation follow-up papers from IMAGE 2023 and IMAGE 2024
Date Submitted by the Author:	21-Feb-2025
Complete List of Authors:	Omar, Samara; Colorado School of Mines, Geophysics Simmons, James; Colorado School of Mines, Geophysics Calderón-Macías, Carlos; TGS
Keywords:	multicomponent, ocean-bottom node, illumination, imaging, 3C
Subject Areas:	Interpretive processing/modeling, Interpretation concepts, algorithms, methods, and tools, Other

Contributions of the Horizontal OBN Components to P-wave Imaging

Samara Omar[1], Jim Simmons[1] and Carlos Calderón-Macías[2]

Department of Geophysics, CSM[1], TGS[2]

Corresponding author email: somar@mines.edu

Original paper date of submission: 9.24.2024

Revised paper date of submission: 2.21.2025

Final submission: 4.29.2025

Submission to Special Section:

"Geological and geophysical interpretation follow-up papers

from IMAGE 2023 and IMAGE 2024"

Portions of this work have been presented at IMAGE 2023 and IMAGE 2024.

ABSTRACT

Horizontal (H) components of ocean bottom node surveys are acquired at no additional cost to the extensively analyzed vertical (Z) and pressure components. Despite this, H components are seldom processed for reflected converted compressional (P) to shear waves (PS-waves), and less so for reflected P waves (PP) due to a perceived lack of value relative to the added processing cost. Recent advancements in elastic migration methods have sparked interest in the H components given a clear rationale for enhancing PS imaging and interpretation through joint migration. Conversely, the potential benefits of the PP energy observed on the H components (HPP data) are less understood. We investigate the foundational characteristics of HPP data and its contribution to P-wave imaging using idealized acoustic synthetic datasets, free of PS-data and surface-related multiples. HPP illumination varies with respect to bed structure (e.g., dips and depth) like traditional Z component P-wave (ZPP) data but is more sensitive to acquisition geometries. Specifically, we present observations of polarization and strong illumination biases to signed-offsets which motivate a need for strategic handling of HPP data in processing flows. Using partial-offset stacks, we demonstrate that HPP data enhances traditional ZPP imaging most effectively for shallow dipping beds and beneath salt overhangs where inter-salt multiples complicate the ZPP image. Our results elucidate the broader need for studying the sensitivities of all component data prior to joint processing, and more specifically present new understandings of how HPP data can be optimally employed to reduce the uncertainties of traditional ZPP imaging.

INTRODUCTION

Ocean-bottom node (OBN) surveys in offshore exploration, compared to traditional surface streamer surveys, have the operational advantage of allowing for the acquisition of longer offsets and richer azimuth sampling, both of which aid in velocity model building and imaging of complex geologic settings (Mei et al., 2019; Huang et al., 2023). Additionally, the advantages of acquiring PS-wave information, dominantly recorded on the horizontal (H) components have played a role in the growing interest in OBN surveys. This is driven by the increased feasibility of elastic propagation in imaging which requires leveraging the complete wavefield recorded on all components of OBN data. Studying the sensitivity of each component (pressure, vertical (Z), and H) to all wave modes is an important first step to understanding possible advantages or pitfalls in the use of multi-component (MC) data required for elastic workflows.

H components of OBN surveys are often used in preprocessing procedures for example, in sensor orientation which uses all components (e.g. Gaiser (1998) and Dellinger et al. (2002)) and for specialized applications such as simultaneous source deblending (Jennings and Ronen, 2017) that use signal polarization as additional statistics for source separation. In terms of interpretation, noteworthy applications of the H components leverage the PS signal where sufficiently recorded in specific geologic conditions. Examples include gas cloud imaging (Nahm and Duhon, 2003), shear wave splitting for fracture characterization (Lou et al., 2001), hydrocarbon validation using joint inversion (e.g. Damasceno et al. (2021) and Cafarelli et al. (2006)) and, shear wave velocity model building using full waveform inversion (e.g. Vigh et al.

(2014); Masmoudi et al. (2021) and Dhelie et al. (2022)). In sparse OBN surveys, PS-wave interpretation can be hampered by poor subsurface illumination caused by a coarse sampling of the receivers and potentially lower signal-to-noise (e.g. Ata et al. (2013), Casasanta and Gray (2015) and Holden et al. (2016)).

Reflected P-wave (PP) energy recorded on the H components (HPP data) has been largely overlooked. In addition to the drawbacks associated with sparse acquisition previously mentioned, there are at least two historical factors that have likely discouraged analyzing HPP data. First is the expectation that the PP signal is dominantly polarized in the Z direction due to the mostly positive velocity gradient in the subsurface. This hypothesis is possibly valid in flat layered geology but in structurally complex regions which have historically been surveyed with short offset, narrow azimuth acquisitions, the observed lack of HPP data is likely due to the limited aperture. Zhao (2008) presents several 3-C acquisition case studies (albeit on land) where HPP signal can be observed on the H component shot gathers. We refer the reader specifically to Figures 1 and 8 in Zhao (2008). Similarly, the OBN acquisition presented in Zhang et al. (2021)'s field study reveals strong HPP energy on the MC shot gathers. Both field-data publications focus on the value of the PS information recorded on the H components (HPS data) and treat the HPP data as coherent noise. Along this vein, when targeting only the HPP data, the HPS data translates as coherent noise. This is the second factor limiting the exploitation of HPP data, as it is potentially masked by the strong PS signal. Despite this, Liu and Simmons' (2024) brief presentation of HPP images generated from an elastic simulation of the SEAM II Barrett model, is a motivating example for our investigation. This study is focused on identifying and understanding the distinctive behavior of HPP data, and as such, we strategically do not model the shear modes. Although our preliminary acoustic experiment simplifies MC field data considerably, it effectively characterizes geological scenarios where integrating HPP data into migration algorithms could yield substantial benefits.

In practice, P-wave imaging procedures may begin with summing the pressure and Z components (i.e. PZ summation) for separating the up- and down-going energy at the ocean floor (Seher et al., 2022), and for removing shear wave energy (Yang et al., 2020). The downgoing wavefield is particularly beneficial for near-surface imaging when mirror migration methods are implemented (Wang et al., 2010). These PZ summations require assumptions in scaling the energy of the Z component data, based on the emergence angle, such that the unwanted wave modes cancel out (Soubaras, 1996). Thus, although the pressure component arguably detects P waves from all angles, the downgoing wavefield used in imaging and interpretation emphasizes the events detected on the Z component. This rationale motivates our experimental decision to not simulate free-surface effects. That is, acknowledging that PZ summation focuses working datasets to P-waves on the Z component (ZPP data), we model the upgoing wavefields and focus our analysis on the Z and H components. It is worth mentioning that given this upgoing-only wavefield simulation, the insights into ZPP versus HPP data presented in this study apply to 3-component land data as well.

The paper begins by introducing the 2-D synthetic models used to simulate the idealized acoustic, OBN datasets. The choice of the Kirchhoff prestack depth migration algorithm for imaging is then justified, with details provided on the parameterization and handling of OBN geometries. Each case study is analyzed individually, with the analysis centering on the use of partial stack images to evaluate the characteristics and contributions of HPP versus ZPP illumination. This is followed by a summary of the generalized characteristics of HPP data, offering new insights into the handling and utilization of H component data, which are further discussed before concluding remarks are presented.

NUMERICAL MODELS AND SIMULATIONS

We simulate OBN acquisitions on two familiar industry models - the shallow water, faulted setting of the 2-D Marmousi2 model (Martin et al., 2002) and a 2-D section of the deepwater, salt model published by SEG SEAM (Fehler and Keliher, 2011). The Marmousi2 model is a 17 km x 3.5 km cross-section representative of the North Quenguela Trough in the Cuanza Basin, Angola. We show the P-wave velocity and density models for this case study in **Figures 1A** and **1B** respectively. It is an elastic extension of the acoustic Marmousi model and allows for easy extension of this work with elastic simulations. To simulate a best-case scenario for HPP imaging, the Marmousi2 model was modified to replace the shallow transition layers at the seafloor with a water layer. The ocean bottom data were thus recorded on the new seafloor at a depth of 0.512 km. The grid and cell sizes of the model are 4250 x 875 and 4 m x 4 m respectively. The SEAM Phase 1 model is analogous to a complex salt domain in the Gulf of Mexico and the extent of the 2-D cross-section is 17.5 km x 7 km. The P-wave velocity and density models for this case study are shown in **Figures 1C** and **1D** respectively. The grid and cell sizes of the model are 1751 x 1401 and 10 m x 5 m respectively. Compared to the Marmousi2 model, the seafloor depth varies from 500m to 1000m. OBN geometries for both models were simulated by placing receivers every 25 m at the water-solid interface. Sources were characterized by a symmetric, 15 Hz Ricker wavelet and were spaced 25 m at a constant depth of 10 m in the water column.

To effectively highlight the kinematics of the HPP data, we forward model the acoustic wave equation without implementing the standard free-surface condition to forestall the generation of PS-waves and surface-related multiples. We simultaneously model the pressure, Z- and H-displacement wavefields by solving a system of two coupled first-order equations respectively describing the vector displacement and scalar pressure fields. These equations were iteratively solved using a forward-marching, staggered in time finite-difference scheme implemented with the Devito software package (Louboutin et al., 2019; Luporini et al., 2020).

COORDINATE SYSTEM FRAMEWORK

At any receiver, the detected signal's polarity depends on both the coordinate system convention and subsurface properties i.e. layer geometries and elastic properties. We assume an acquisition coordinate system in which the positive Z and X directions point upward and to the right, respectively. Assuming a horizontally-layered Earth model with OBN acquisition (**Figure 2**), an upgoing reflected wave is detected as a positive displacement in Z whereas a downgoing direct wave is detected as a negative displacement in Z. Receivers located to the right of the source are designated as positive-offset receivers, while those to the left are considered negative-offset receivers. For particle motion recorded along the X direction, positive-offset receivers detect positive displacements in X and negative-offset receivers detect negative displacements. This reversal of horizontal particle motion at zero-offset is realized as opposite polarities on the recorded X-component shot gathers and is hereon referred to as a ‘signed-offset polarization bias’ (SOP bias).

We show an example of the Z and X-component shot gathers at 3.0 km on the Marmousi2 model (**Figures 3A** and **3B**) where the stratigraphy is fairly flat. All energy observed on these gathers are P-wave due to the acoustic forward modeling. For the flat layered stratigraphy at near offsets, this PP energy is dominantly recorded on the Z component, and at far offsets, the energy is distributed onto both the Z and X components. As expected by the coordinate system definition, the direct wave (yellow arrow) is recorded with negative polarity on all offsets of the Z component gather and the negative offsets of the X component gather. On the positive offsets of the X component, this direct wave is recorded with positive polarity. The strong signal at ~.8s (blue arrows) is a reflected P-wave from the top of a gas reservoir and should have a negative amplitude because of the negative impedance contrast. This reflection is recorded as negative polarity on all offsets of the Z component and on the positive offsets of the X components. On the negative offsets of the X components, the recorded signal has a positive polarity.

The use of a radial-transverse (R-T) horizontal coordinate system successfully removes this SOP bias for reflectors parallel to the recording surface. The R direction for any source-receiver pair points along the source-to-receiver azimuth (Gaiser, 1999). **Figure 3C** shows the result of this rotation at 3.0 km. The direct wave and reflected gas-pocket signal are detected as positive and negative polarities respectively regardless of signed-offset. Where subsurface layers are dipping, the conversion to the R-T system imposes a SOP bias. This is observed on the shot gathers at 9.3 km of the Marmousi2 model where the layers are severely tilted and faulted. In

Figures 3D-3F, we show the Z, X and R shot gathers and annotate the X and R components with pink arrows to highlight the SOP observations.

Stacking across signed offsets in either the X or the R direction, can potentially distort or cancel signal depending on the target bed geometry. As rotation to R-T is a standard industry practice, our initial analyses include a cross-examination of both the X and R component data where the forward modeled 2-D data is rotated to the R direction prior to migration.

MIGRATION ALGORITHM

The selection of a migration algorithm can be streamlined into choices between ray-based versus wavefield-based, and vector-based versus scalar-based migrations. Ray-based migrations such as Kirchhoff prestack depth migration (KPSDM) are computationally inexpensive compared to wavefield-based approaches such as reverse time migration (RTM). Furthermore, obtaining 'true' relative amplitude gathers is more efficient and straightforward with KPSDM compared to RTM. For these trivial reasons, KPSDM remains an industry standard in most geologic regimes or at the very least, employed in fast-track processing in regions with complex subsurface structures. Another benefit to ray-based approaches is the ease of migrating distinct wave modes controlled by the input travel time field estimations i.e. scalar wavefield migration (Bucha, 2021). While this distinctive imaging is possible in wavefield-based migrations, the severe cross-talk of unwanted wave-modes often require wavefield separation (effectively migrating each wavefield with a scalar algorithm e.g. Yan and Sava (2009)) or an advanced imaging condition (treating the problem as a vector-based joint migration e.g. Hou and Marfurt

(2002) and Rocha et al. (2016)). Vector-based migrations of elastic data often utilize the MC datasets and produce separate P- and S-wave images. These vector approaches may be implemented in both ray-based or wavefield-based migrations (Hokstad, 2000). The interest in vector-based, elastic reverse time migrations (ERTM) in structurally-complex, marine environments is increasing due to more activity in ocean-bottom surveys which facilitate PS-wave acquisition. This is motivated by the need for time-lapse studies of reservoir conditions requiring both P- and PS-wave information. Although the H components are valued for the PS-wave data in joint processing workflows, it is poorly understood how the HPP data impact vector-based migrations of P-wave data. Thus, we use a scalar-based KPSDM such that the P-wave information on each component was separately imaged and the independent contributions of ZPP versus HPP data can be assessed. We continue the discussion of migration algorithms in the 'Suggestions for Further Investigation' section considering the results presented.

The specific KPSDM code used (written by Liu (1993) and found in Seismic Unix (SU) (Stockwell Jr, 1999)) is based on Bleistein et al. (1987)'s integral formulation which is kinematically accurate for direct pure-mode and converted-wave modes (Bleistein, 1986). Our analysis emphasizes subsurface reflection point illumination differences of the ZPP and HPP images and not on reflection amplitude differences. All components were migrated with the same ray tracing and migration parameterizations. The code was modified to utilize two distinct travel time fields for sources and receivers having different elevation datums. This modification makes the Kirchhoff code directly suitable for ocean-bottom geometries. Source-side and receiver-side travel time tables for input to the KPSDM were calculated using a 2-D paraxial ray tracing algorithm (Liu, 1993). We performed ray tracing on a smoothed version of the true P-wave velocity models for both case studies. Turning rays were not migrated. Maximum offsets recorded for the Marmousi2 and SEAM Phase 1 models were 3000 m and 5000 m respectively and a migration aperture equal to these maximum recorded offsets was used for both case. Prior to stacking, data were migrated into common image gathers (CIGs) at 0.1 km offset bins with a 45^{o} outside mute and mild bandpass filter.

RESULTS: MARMOUSI2 CASE STUDY

The Marmousi2 model provides a convenient opportunity to begin analyzing HPP illumination for flat versus tilted stratigraphy. **Figure 4** presents the Z, X and R CIGs at the two shot gather locations shown in **Figure 3** (upper and lower rows). At both locations, the migrated PP reflections on the X and R CIGs are flattened similar to that of the Z component (blue arrows). The SOP bias observed in the X and R component shot gathers in **Figure 3** persists in the CIGs—at 3.0 km, rotation to R corrects the X-component SOP bias, whereas at 9.3 km, the rotation instead introduces an SOP bias.

A closer examination of the 9.3 km CIGs reveals a signed-offset illumination (SOI) bias on the H components (both X and R) which were not immediately obvious on the shot gathers. Specifically, some steeply dipping beds that are uniformly illuminated across all offsets on the Z component exhibit differences in amplitude and resolution between positive and negative offsets on the X and R components (refer to pink arrows in **Figures 4D-F**). This SOI bias, which exists on some reflections regardless of horizontal coordinate system, underscores the importance of understanding how images and interpretations differ between positive- and negative-offset stacks of the H component data. In the remaining analyses of this work, we focus on the R components for reasons outlined in the 'Coordinate System Framework' section.

Partial-offset stacks are generated with the following angle ranges: $0^o - 10^o$ ultra-near, $10^o - 20^o$ near, $20^o - 30^o$ mid, $30^o - 45^o$ far. These angles (θ in **Figure 2**) are computed as the emergent angles assuming flat model layers. **Figure 5** compares partial-offset stacks of the RPP data, specifically ultra-near versus mid-offset stacks in the most structurally complex area of the model. At ultra-near offsets, dips are similarly illuminated on both positive and negative offset stacks (**Figures 5A** and **B** respectively) while at the respective mid offsets (**Figures 5C** and **5D**), the SOI bias is stronger. These observations are annotated with yellow arrows noting that on mid offset stacks, the left-dipping events are better imaged on the negative offset stack.

Our analysis of the Marmousi2 synthetic OBN data reveals two key findings about H component records, independent of the chosen coordinate system: (1) polarization and (2) illumination varies systematically between positive and negative offsets, depending on subsurface geometry. Notably, receivers positioned downdip relative to a given reflector capture stronger HPP energy, highlighting the importance of partial-offset HPP stacks when imaging uniform dips. To explore how this data can complement traditional ZPP interpretation, we now turn to a salt imaging study—a common industry challenge in the pursuit of salt-juxtaposed reservoirs.

RESULTS: SEAM PHASE 1 CASE STUDY

Imaging subsalt and salt flanks in marine environments are often difficult because of sparse illumination. The SEAM example investigates the value of HPP illumination to resolving such subtle salt-edge features using partial-offset images generated using the same angle ranges as in the Marmousi2 example.

Figure 6 compares the full (ultra-near to far), signed-offset stacks of the migrated ZPP and RPP data. Although the migration did not incorporate turning ray information necessary for imaging a continuous base of salt, the RPP images show a more focused base of salt reflector wherever it is illuminated in comparison to the corresponding ZPP images (yellow arrow annotations). This is partly attributed to the strong interference of poorly migrated inter-salt multiples on the ZPP images (blue arrows on **Figures 6A** and **6B**). Although some multiples are observed on the RPP images (blue arrows on **Figures 6C** and **6D**), they are relatively weak compared to the primary reflections.

Similar to the Marmousi2 observations, the SOI bias of the RPP data are more pronounced in the RPP data (compare **Figures 6C** versus **6D**) than in the ZPP data (compare **Figure 6A** versus **6B**). We also note that negative offset RPP data best illuminates left-dipping sediment layers (on the left side of the salt body in **Figure 6D**) and vice versa for right-dipping sediment layers (on the right side of the salt body in **Figure 6C**), and that multiple contamination on RPP differs between signed-offset images.

In deepwater settings, prolific hydrocarbon reservoirs are often trapped against salt flanks and beneath salt overhangs. **Figure 7** examines the imaging of the right flank with positive, partial-offset stacks (red box #1 on **Figure 6A**) and **Figure 8** examines the left flank with negative, partial-offset stacks (red box #2 on **Figure 6A**).

The regions where RPP illumination enhances areas of poor ZPP salt flank imaging vary across the dataset. For example, the right dipping salt flank (annotated on a few panels in **Figure 7** with dotted yellow arrows) is similarly and continuously imaged on all ZPP and RPP partial-offset images however, the shallow salt edge (solid yellow arrow annotations), benefit more from RPP illumination than ZPP (particularly at mid to far offsets). Additionally, in some instances, the overhang reflector is better focused on the RPP image compared to the corresponding ZPP image. Such examples on **Figures 7** and **8** are annotated with blue arrows and in particular, the continuity of the overhang on the RPP image in **Figure 8E** is a convincing example of the relevance of the RPP illumination to imaging even at near offsets.

Similar to the discontinuous salt flank imaging, the imaging of dipping beds that are weakly illuminated on ZPP can be supplemented by the RPP illumination of these reflectors. Dotted white arrows on **Figures 7** and **8** highlight a few such reflectors at all offsets.

Under the salt overhangs, solid white arrows annotate unique observations where the inter-salt multiples contaminate the ZPP images more than the RPP data. An additional noteworthy observation is that in some scenarios where these inter-salt multiples are recorded on the R component, they are inverted polarity to the recorded polarity on the Z component. For example, compare the highlighted multiple in **Figure 7A** versus **7E**.

Assuming that the SOP biases can be remedied with a vector-based migration, then stacking the ZPP and RPP data can provide several benefits to salt basin imaging which include improving the illumination of steeply dipping reflectors (such as salt flanks and salt-juxtaposed beds) and suppressing multiple interference under overhangs. Using both the ZPP and RPP data potentially improves the resolution of salt-sediment interfaces which improves the interpretation of potential trapping and sealing mechanisms critical for accurate hydrocarbon prospecting.

SUMMARY OF OBSERVATIONS

We observe that the reflected P-wave data recorded on the H component contains sufficient signal that after migration, illuminates dipping reflectors differently, but complimentary, to the Z component illumination. The strength of the HPP signal is a function of target depth and dip relative to receiver depth and offset. When P-wave signal is strongest on the H component, it is weakest on the Z component and there is potential benefit to jointly analyzing or combining both components. From both studies, we generalize the following observations regarding the reflected P-waves:

A. RPP polarities of dipping beds are biased to signed-offset (SOP bias) i.e. a dipping interface will be detected with opposite polarities on the negative- versus the positive-offset receivers, which leads to potentially destructive inference in stacking across signed-offsets.
B. HPP illumination of dipping beds are biased to signed-offset (SOI bias) regardless of coordinate system (X or R). More specifically, beds dipping in the source-to-receiver (offset) direction are best illuminated by receivers positioned on the downdip side of the source.
C. HPP illumination of the subsurface varies with depth and dip of bed (related to the emergence angle of the reflected wave), and absolute source-receiver offset
    a. In the simple Marmousi2 study, these relationships are discernible: Shallow,

dipping beds are best illuminated at near offsets on both signed-offset H components

b. In the complex SEAM Phase 1 salt study, these relationships are less intuitive and the strength of HPP sub-salt and salt-flank imaging vary possibly due to velocity complexity.

DISCUSSION AND SUGGESTIONS FOR FURTHER INVESTIGATION

Evaluating the sensitivities of the H components to individual wave modes is crucial for the efficient implementation of joint imaging and analysis of MC data. Our synthetic experiments provide evidence of the value of HPP data, even at small offsets, to imaging shallow and/or complex subsurface structures. This not only has a potential impact on resource mapping e.g., in deepwater salt field or shallow gas hydrate (Backus et al., 2006) exploration but also on shallow hazard mapping for well-planning or other geotechnical seafloor projects.

The choice of acoustic experiments has allowed us to establish a fundamental understanding of HPP data in isolation from other wave modes. Repeating these analyses on elastic datasets or with free-surface effects are natural progressions of this work. Based on our observations of strong biases in HPP illumination towards signed-offsets, we anticipate similar biases in the case of free-surface multiples and PS-waves in elastic media.

The use of KPSDM in this study presents both advantages and limitations. KPSDM is widely used for its efficiency and adaptability, however its reliance on a ray-based imaging model limits proper migration to only single-point reflection events. In regions with strong velocity contrasts and/or complex 3D structural geology, KPSDM of multiple reflections and refractions can result in artifacts. While these limitations may introduce uncertainties in the interpretation, they do not diminish the significance of our key observations. The systematic SOP and SOI biases remain fundamental aspects of the recorded HPP wavefield, independent of the imaging method. It is possible, however, to resolve these biases by accounting for the direction of emerging particle motion relative to the receiver directions. Exploring such imaging methods could help assess the robustness of these findings.

Correcting the SOP concerns (associated with item A in the summarized observations) would allow for comparison of amplitudes in the ZPP and HPP images. This has been discussed and exemplified in Kirchhoff migration applications of 3D VSP data (Dillon, 1990; Gherasim et al., 2005) and multi-channel teleseismic receiver functions (Bostock, 2002; Millet et al., 2019). Implementation of vector-based migrations such as the vectorial-based Kirchhoff migrations as presented by Kuo and Dai (1984) or RTM using the energy-norm imaging condition by Rocha et al. (2016) can also account for these amplitude variations with emergence angle. A comparison of these vector-based migrations on separated signed-offset data has the potential to produce better images by capitalizing on the signed-offset biases of the HPP data.

Regarding multiples, our results have demonstrated weaker inter-bed salt multiples on HPP compared to ZPP. It is thus important that these strong ZPP multiples are sufficiently attenuated prior to joint migration otherwise the contributions of the HPP data in critical regions, such as under salt overhangs and along flanks, may be masked by the cross-talk related to these coherent noise events. In instances where inter-bed multiples are discernible on RPP data, there is potential to leverage the observation of opposite polarities between ZPP and RPP to identify and suppress these undesirable modes. We hypothesize that surface-related multiples would also weakly impact HPP data, as they tend to propagate more vertically. Where such multiples are recorded on the HPP data, there may be an opportunity to perform a summation of pressure, Z, and H component data to achieve a more accurate wave mode separation which requires estimations of emergence angles (Schalkwijk et al., 2003).

For velocity model building (VMB), although not in the scope of this work, it is apparent from the results presented that using reflected P-wave energy captured in the H component could benefit the P-wave VMB particularly for shallow geology. Solano and Plessix (2023) have demonstrated the value of a joint elastic full waveform inversion (EFWI) using both the Z and pressure components, versus individual inversions of either component. Although the pressure component is omnidirectional, the joint inversion benefits from the SNR of the unidirectional Z component P-wave records. The higher SNR reflected P-wave signal from the H component can similarly benefit EFWI workflows. Another plausible method to improving VMB is including the residual moveout picks of the P-signal from the HPP migrated gathers to the conventional picks from the Z component. With no considerable cost, this potentially improves P-wave model updating without the need for addressing noise in the pre-stack data before migration. Cho et al. (2022) addressed the utility of the H component for the shallow shear VMB in salt fields of the Gulf of Mexico. A potential research opportunity following from our results is investigating the PS-signal recorded on the Z component and exploring its value to shallow shear VMB which suffers from sparse receiver acquisition.

CONCLUSIONS

P-wave energy measured on H components has been mostly neglected in MC surveys. We analyze this HPP data for image improvements evidenced by enhanced focusing and continuity of reflectors versus using a single Z component dataset. Using ’best-case’ acoustic simulations of OBN acquisitions on widely used industry marine models, we demonstrate the added value of HPP illumination, particularly for imaging shallow and dipping subsurface geometries.. We make critical observations about signed-offset polarization and illumination biases in HPP data compared to ZPP data, with these effects becoming more pronounced at steeper dips and shallower depths. HPP images complement and reduce the uncertainty of the ZPP interpretation of shallow, steeply dipping beds or salt flanks, and intriguingly in regions below salt overhangs where inter-salt multiples complicate the ZPP image. Results shown have potential implications for model building methods, and in particular for the incorporation of components in tomography and FWI approaches. Including free-surface multiples and converted waves in more complex simulations is a necessary succession of this research which will address the complexities in MC imaging of field data.

ACKNOWLEDGEMENTS

We would like to thank the sponsors of the Reservoir Characterization Project for their financial support and fruitful discussions. We extend our sincere thanks to our reviewers, including Dr. Gaiser and Dr. Liu, for their insightful feedback and constructive comments.

DATA AVAILABILITY STATEMENT

The open-source tools Devito (for forward modeling) and Seismic Unix (for data processing and migration) can be accessed at their respective websites: https://www.devitoproject.org and https://wiki.seismic- unix.org/start. Additionally, the synthetic models used in this study are publicly accessible. The Marmousi2 model is hosted at https://wiki.seg.org/wiki/AGL Elastic Marmousi, while the SEAM Phase1 model is available at https://seg.org/seam/open-data. For the simulated OBN data and processing scripts, interested parties can request access from the corresponding author.

CONFLICT OF INTEREST

The authors declare that there is no conflict of interest regarding the publication of this paper.

REFERENCES

Ata, E., R. Olson, C. C. Mosher, S. Shaw, and S. Betterly, 2013, A look at converted waves from an OBN test survey: Presented at International Exposition and Annual Meeting, SEG.

Backus, M. M., P. E. Murray, B. A. Hardage, and R. J. Graebner, 2006, High-resolution multicomponent seismic imaging of deepwater gas-hydrate systems: The Leading Edge, 25, 578–596.

Bleistein, N., 1986, Two-and-one-half dimensional in-plane wave propagation: Geophysical Prospecting, **34**, 686–703.

Bleistein, N., J. K. Cohen, and F. G. Hagin, 1987, Two and one-half dimensional born inversion with an arbitrary reference: GEOPHYSICS, **52**, 26–36.

Bostock, M., 2002, Kirchhoff-approximate inversion of teleseismic wavefields: Geophysical Journal International, **149**, 787–795.

Bucha, V., 2021, Kirchhoff pre-stack depth scalar migration in a simple triclinic velocity model for three-component P, S1, S2 and converted waves: Geophysical Prospecting, **69**, 269–288.

Cafarelli, B., S. Randazzo, S. Campbell, J. F. F. Sobreira, M. A. G. Guimaraes, C. Rodriguez, P. Johann, and C. Theodoro, 2006, Ultra-deepwater 4-C offshore Brazil: The Leading Edge, **25**, 474–477.

Casasanta, L., and S. H. Gray, 2015, PS imaging of ocean-bottom data: The Leading Edge, **34**, 414–420.

Cho, Y., C. Pérez Solano, J. Kimbro, Y. Yang, R.-E´ . Plessix, and K. Matson, 2022, Influence of shear velocity on elastic full-waveform inversion: Gulf of Mexico case study using multicomponent ocean-bottom node data: GEOPHYSICS, **87**, R391–R400.

Damasceno, A., A. Tura, and J. Simmons, 2021, The added value of joint PP-PS inversion for reservoir characterization: A case study using Jubarte PRM seismic data (offshore Brazil): Geophysical Prospecting, **70**, 121–134.

Dellinger, J., R. Clarke, and P. Gutowski, 2002, Three-dimensional vector infidelity correction by general linear transform: Presented at 64th EAGE Conference & Exhibition, European Association of Geoscientists & Engineers, cp–5.

Dillon, P. B., 1990, A comparison between Kirchhoff and GRT migration on VSP data: Geophysical Prospecting, **38**, 757–777.

Eivind Dhelie, P., V. Danielsen, J. Andre Haugen, E. Davenne, K. Richard Straith, A. Roodaki, M. Peiro, A. Fotsoh, W. Gao, N. Masmoudi, et al., 2022, High-resolution FWI of converted-wave data—a case study from the Edvard Grieg field: Presented at International Exposition and Annual Meeting, SEG, D011S042R003.

Fehler, M., and P. J. Keliher, 2011, Seam phase 1: Challenges of subsalt imaging in tertiary basins, with emphasis on deepwater Gulf of Mexico: Society of Exploration Geophysicists.

Gaiser, J.E., 1998, Compensating OBC data for variations in geophone coupling: 68th Annual

International Meeting, SEG, Expanded Abstracts, 1429-1432.

Gaiser, J., 1999, Applications for vector coordinate systems of 3-D converted-wave data: The Leading Edge, **18**, 1290–1300.

Gherasim, M., C. Hoelting, and K. Marfurt, 2005, 3-D VSP elastic Kirchhoff pre-stack depth migration - Vinton dome, Louisiana: International Exposition and Annual Meeting, SEG, Expanded Abstracts, 2649–2652.

Hokstad, K., 2000, Multicomponent Kirchhoff migration: GEOPHYSICS, **65**, 861–873.

Holden, J., D. Fritz, O. Bukola, J. McLeman, R. Refaat, C. Page, J. Brunelliere, S. Sioni, A. Mitra, and X. Lu, 2016, Sparse nodes and shallow water - PS imaging challenges on the Alwyn north field: 78th EAGE Conference and Exhibition 2016, EAGE, Expanded Abstracts, 1–5.

Hou, A., and K. J. Marfurt, 2002, Multicomponent prestack depth migration by scalar wavefield extrapolation: GEOPHYSICS, **67**, 1886–1894.

Huang, H., T. Wang, and J. Cheng, 2023, PS-wave separation of multicomponent seismic data at the land surface based on deep learning: GEOPHYSICS, **88**, V233–V247.

Jennings, J., and S. Ronen, 2017, Simultaneous source deblending with the radiality and source-similarity attributes: Presented at International Exposition and Annual Meeting, SEG.

Kuo, J. T., and T.-f. Dai, 1984, Kirchhoff elastic wave migration for the case noncoincident source and receiver: GEOPHYSICS, **49**, 1223–1238.

Liu, Y., and J. Simmons, 2024, Depth imaging of multicomponent seismic data through the application of 2D full-waveform inversion to P-and SH-wave data: SEAM II Barrett model study: Geophysical Prospecting.

Liu, Z., 1993, A Kirchhoff approach to seismic modeling and prestack depth migration: International Exposition and Annual Meeting, SEG, Expanded Abstracts, 888–891.

Lou, M., Y. Zhang, and L. D. Pham, 2001, Shear-wave splitting and fracture orientation analysis from PS waves-examples from synthetic and field OBC data: Presented at International Exposition and Annual Meeting, SEG.

Louboutin, M., M. Lange, F. Luporini, N. Kukreja, P. A. Witte, F. J. Herrmann, P. Velesko, and G. J. Gorman, 2019, Devito (v3.1.0): an embedded domain-specific language for finite differences and geophysical exploration: Geoscientific Model Development, **12**, 1165–1187.

Luporini, F., M. Louboutin, M. Lange, N. Kukreja, P. Witte, J. Hu¨ckelheim, C. Yount, P. H. J. Kelly, F. J. Herrmann, and G. J. Gorman, 2020, Architecture and performance of Devito, a system for automated stencil computation: ACM Trans. Math. Softw., **46**.

Martin, G. S., S. Larsen, and K. Marfurt, 2002, Marmousi-2: An updated model for the investigation of AVO in structurally complex areas: Presented at International Exposition and Annual Meeting, SEG.

Masmoudi, N., A. Ratcliffe, M. Wang, Y. Xie, and T. Wang, 2021, A practical implementation of converted-wave reflection full-waveform inversion: 82nd EAGE Annual Conference &

Exhibition 2021, EAGE, Expanded Abstracts, 1–5.

Mei, J., Z. Zhang, F. Lin, R. Huang, P. Wang, and C. Mifflin, 2019, Sparse nodes for velocity: Learnings from Atlantis OBN full-waveform inversion test: Presented at International Exposition and Annual Meeting, SEG, D043S125R004.

Millet, F., T. Bodin, and S. Rondenay, 2019, Multimode 3-d Kirchhoff migration of receiver functions at continental scale: Journal of Geophysical Research: Solid Earth, **124**, 8953–8980.

Nahm, J. W., and M. P. Duhon, 2003, Interpretation and practical applications of 4C-3D seismic data, east Cameron gas fields, Gulf of Mexico: The Leading Edge, **22**, 300–309.

Rocha, D., N. Tanushev, and P. Sava, 2016, Acoustic wavefield imaging using the energy norm: GEOPHYSICS, **81**, S151–S163.

Schalkwijk, K. M., C. P. A. Wapenaar, and D. J. Verschuur, 2003, Adaptive decomposition of multicomponent ocean-bottom seismic data into downgoing and upgoing P- and S-waves: Geophysics, 68, no. 3, 1091–1102.

Seher, T., H. Masoomzadeh, Y. Ren, S. Baldock, and B. Wang, 2022, Deconvolution of upgoing and downgoing wavefields: A data example from the Noaka OBN experiment: Second International Meeting for Applied Geoscience & Energy, SEG/AAPG, 2807–2811.

Solano, C. P., and R. Plessix, 2023, Can elastic waveform inversion benefit from inverting multicomponent data?: The Leading Edge, **42**, 184–189.

Soubaras, R., 1996, Ocean bottom hydrophone and geophone processing: International Exposition and Annual Meeting, SEG, Expanded Abstracts, 24–27.

Stockwell Jr, J. W., 1999, The CPW/SU: seismic unix package: Computers & Geosciences, **25**, 415–419.

Vigh, D., K. Jiao, D. Watts, and D. Sun, 2014, Elastic full-waveform inversion application using multicomponent measurements of seismic data collection: GEOPHYSICS, **79**, R63–R77.

Wang, Y., R. Bale, S. Grion, and J. Holden, 2010, The ups and downs of ocean-bottom seismic processing: Applications of wavefield separation and up-down deconvolution: The Leading Edge, **29**, 1258–1265.

Yan, J., and P. Sava, 2009, Elastic wave-mode separation for VTI media: GEOPHYSICS, **74**, WB19–WB32.

Yang, C., Y. Huang, Z. Liu, J. Sheng, and E. Camarda, 2020, Shear wave noise attenuation and wavefield separation in curvelet domain: Presented at International Exposition and Annual Meeting, SEG, D031S032R006.

Zhao, B., 2008, Application of multi-component seismic exploration in the exploration and production of lithologic gas reservoirs: Petroleum Exploration and Development, **35**, 397-412.

Zhang, D., C. Tsingas, A. A. Ghamdi, M. Huang, W. Jeong, K. K. Sliz, S. M. Aldeghaither, and S. A. Zahrani, 2021, A review of OBN processing: Challenges and solutions: Journal of Geophysics and Engineering **18 (4)**, 492-502.

LIST OF FIGURES (with captions)

Figure 1: P-wave velocity (Vp) and density (Rho) models modified from the Marmousi2 dataset created by Martin et al. (2002) are depicted in panels A and B respectively. Transition layers are removed from the original model which places the seafloor at a depth of 0.512 km. 2D P-wave velocity (Vp) and density (Rho) models extracted from the SEAM Phase 1 dataset created by Fehler and Keliher (2011) are shown in panels C and D respectively. Acquisition geometries for the acoustic finite difference forward modeling of an OBN survey for each model are described in the text.

Figure 2: Description of coordinate system for OBN acquisition. The table describes the polarity of different waves registered on the positive or negative offsets of the pressure, Z, X, and R components.

Figure 3: Raw shot gathers from the Marmousi2 experiment for the Z, X, and R components at 3.0 km (A-C), where the stratigraphy is relatively flat, and at 9.3 km (D-F), where the beds are severely tilted and faulted. Yellow and blue arrows (A-C) highlight the direct arrival and the reflection at the top of a gas reservoir, respectively, for each component. For both direct and reflected waves at this location, we observe uniform polarity at all offsets for the Z component and an SOP on the X component, which is corrected by rotation to the R direction. Pink arrows (E and F) highlight comparative dipping bed reflectors: on the X component, no SOP is

observed, while on the R component, an SOP is introduced due to rotation.

Figure 4: CIGs from the Marmousi2 experiment at shot locations 3.0 km (A-C) where stratigraphy is relatively flat and 9.3 km (D-F) where beds are severely tilted and faulted. The H components (X and R) are gained three times the amplitude of the Z component and all gathers have an outer mute of 45 degrees applied. Using the same parameterizations for KPSDM, the PP energy on all components is equally flattened (blue arrows) at both locations. Pink arrows on the 9.3 km CIGs highlight dipping bed reflections which are uniformly illuminated at all offsets on the Z component, but are illuminated differently between the positive and negative offsets of the X and R components.

Figure 5: Comparison of the RPP ultra-near (upper row) and mid (lower row) partial-offset stacks for both positive (left column) and negative (right column) offsets. All panels are displayed on the same amplitude scale. Yellow arrows highlight left dipping bed reflections which are similarly imaged (disregarding polarity) on the ultra-near stacks but better imaged on the negative mid-offset stacks as a result of the biased HPP illumination to signed-offset.

Figure 6: Comparison of full (0 to 45 degrees), signed-offset stacks for ZPP (upper panels) and RPP (lower panels) data. RPP images are gained two times the amplitude of the ZPP images. RPP illumination has a stronger SOI bias (compare the differences in panels C and D) versus the ZPP illumination (compare the minor differences in panels A and B). In general, RPP data supplement the ZPP data in critical locations below the salt overhangs and at the base of salt.

Yellow arrows highlight the base of salt illumination which is more continuous on the RPP images as opposed to the ZPP images which are more affected by poorly migrated inter-salt multiples. Blue arrows highlight these multiples in regions below the salt and under the salt overhangs. Red boxes #1 and #2 on panel A outline the zoomed regions displayed in Figures 7 and 8 respectively.

Figure 7: Positive partial-offset stacks zoomed to the right salt flank of the SEAM Phase 1 model. Zoomed region is described in Figure 6. Panels A-D show the ZPP ultra-near, near, mid, and far partial-offset stacks respectively and panels E-F show the RPP equivalent stacks. Generally, dotted arrows highlight reflectors that are comparably imaged on both Z and R components whereas solid arrows highlight examples where the RPP illumination is significantly better. Yellow arrows highlight observations related to salt imaging and white arrows highlight observations related to stratigraphy. Refer to the text for relevant details.

Figure 8: Negative partial-offset stacks zoomed to the left edge of the main salt body on the SEAM Phase 1 model. Zoomed region is described in Figure 6. Panels A-D show the ZPP ultra-near, near, mid, and far offset stacks respectively, and panels E-F show the RPP equivalent stacks. Descriptions of arrow annotations are the same as those used in Figure 7.

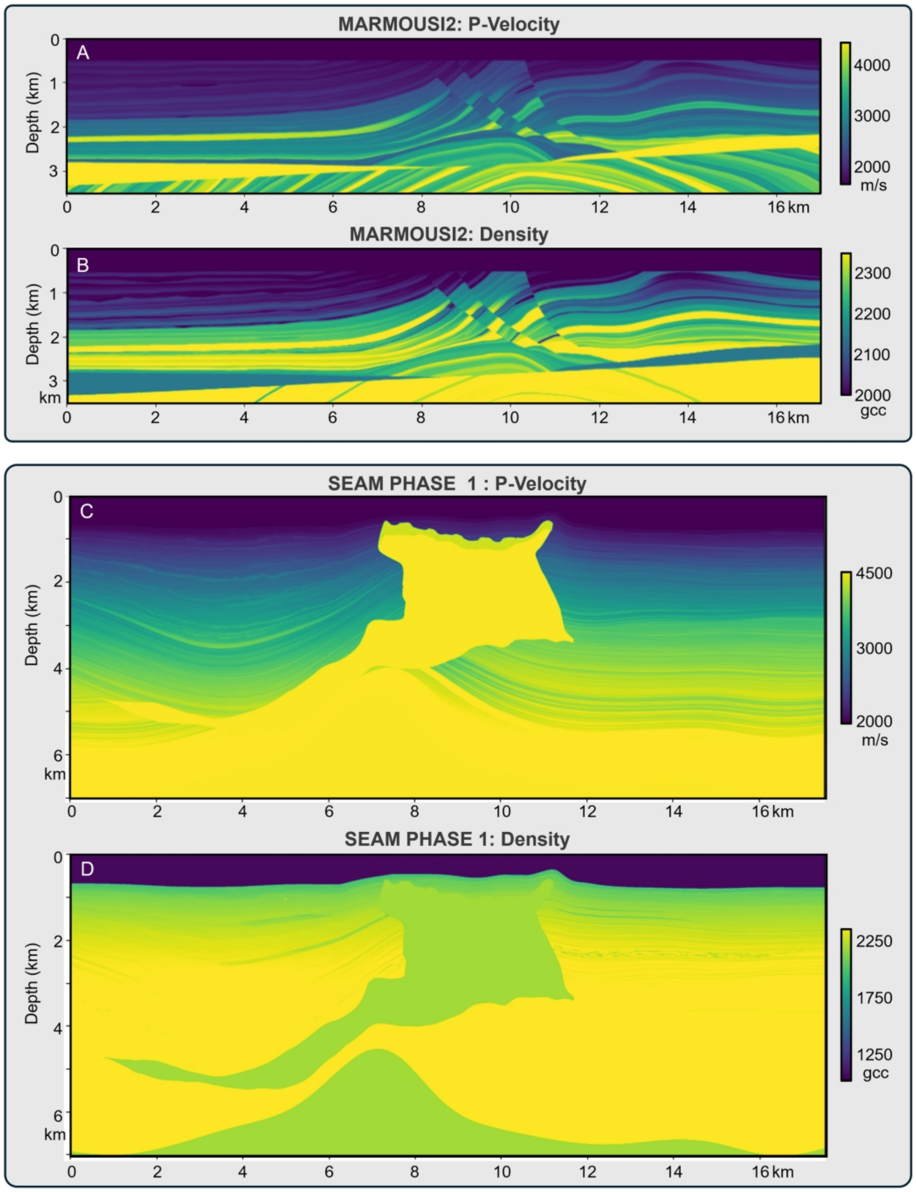

Figure 1: P-wave velocity (Vp) and density (Rho) models modified from the Marmousi2 dataset created by Martin et al. (2002) are depicted in panels A and B respectively. Transition layers are removed from the original model which places the seafloor at a depth of 0.512 km. 2D P-wave velocity (Vp) and density (Rho) models extracted from the SEAM Phase 1 dataset created by Fehler and Keliher (2011) are shown in panels C and D respectively. Acquisition geometries for the acoustic finite difference forward modeling of an OBN survey for each model are described in the text.

193x250mm (300 x 300 DPI)

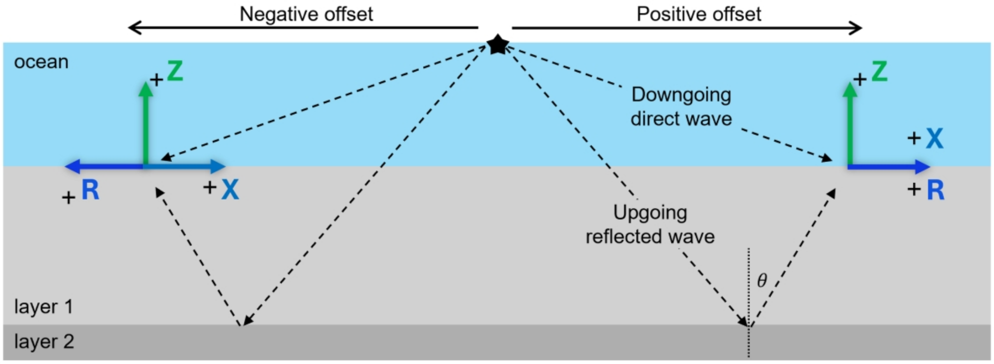

		P	Z	X	R
Downgoing Waves e.g. Direct	Positive Offset	-	-	+	+
	Negative Offset	-	-	-	+
Upgoing Waves e.g., Reflections	Positive Offset	-	+	+	+
	Negative Offset	-	+	-	+

Figure 2: Description of coordinate system for OBN acquisition. The table describes the polarity of different waves registered on the positive or negative offsets of the pressure, Z, X, and R components.

209x129mm (300 x 300 DPI)

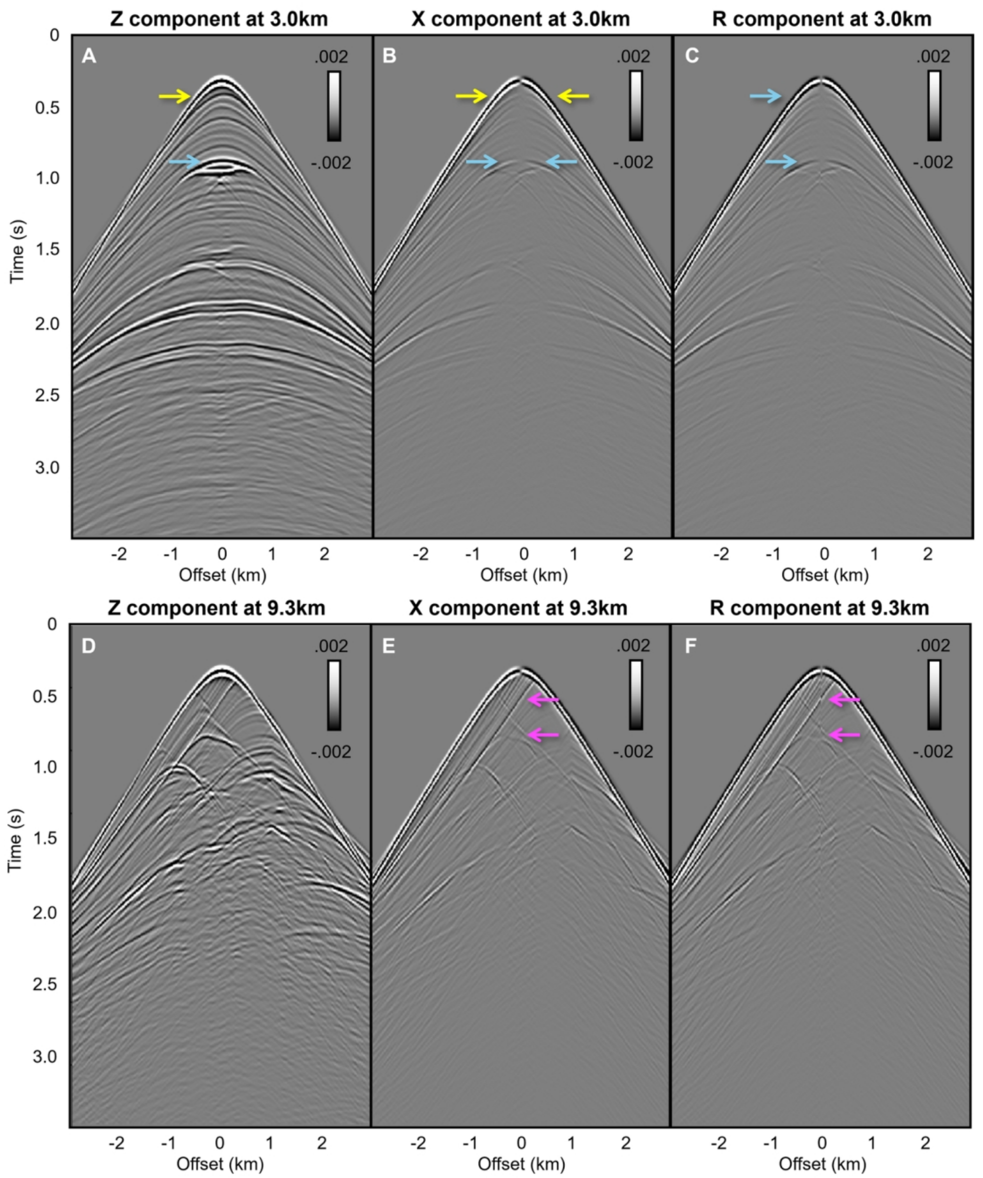

Figure 3: Raw shot gathers from the Marmousi2 experiment for the Z, X, and R components at 3.0 km (A-C), where the stratigraphy is relatively flat, and at 9.3 km (D-F), where the beds are severely tilted and faulted. Yellow and blue arrows (A-C) highlight the direct arrival and the reflection at the top of a gas reservoir, respectively, for each component. For both direct and reflected waves at this location, we observe uniform polarity at all offsets for the Z component and an SOP on the X component, which is corrected by rotation to the R direction. Pink arrows (E and F) highlight comparative dipping bed reflectors: on the X component, no SOP is observed, while on the R component, an SOP is introduced due to rotation.

150x178mm (300 x 300 DPI)

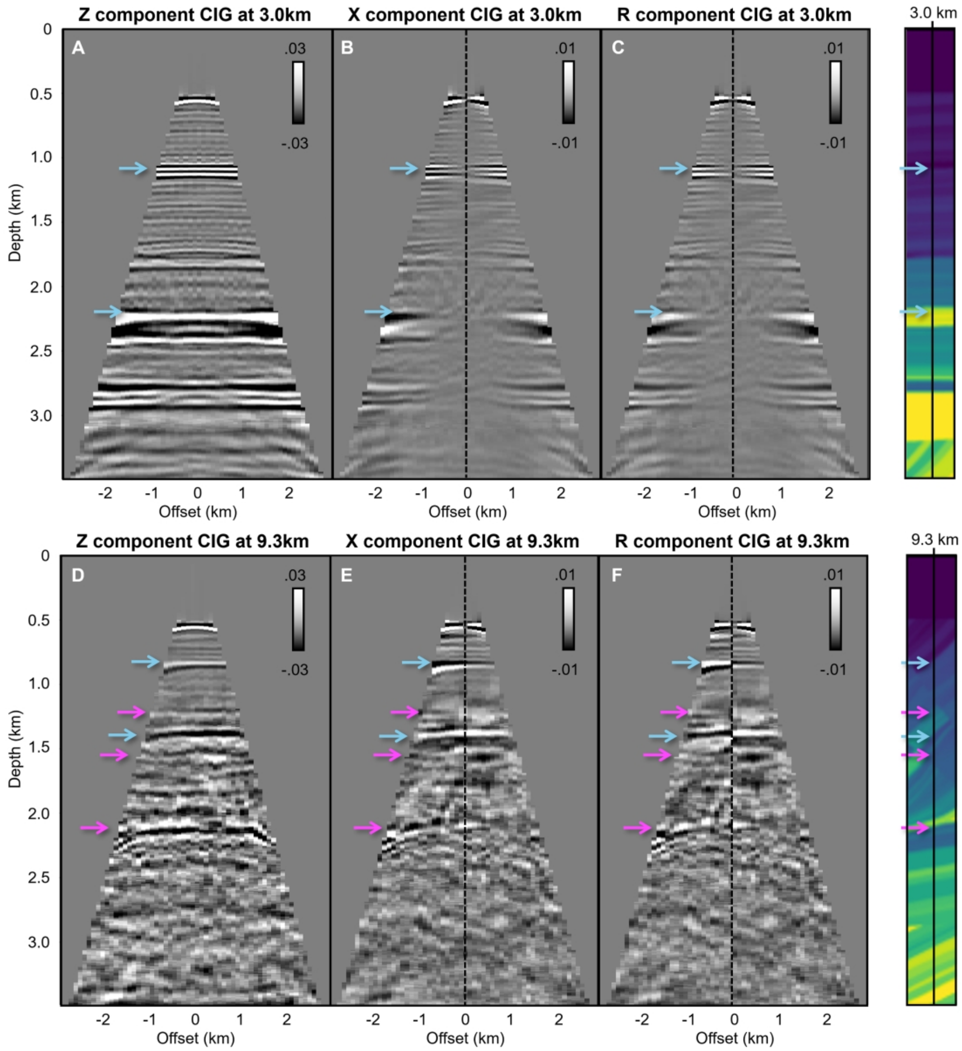

Figure 4: CIGs from the Marmousi2 experiment at shot locations 3.0 km (A-C) where stratigraphy is relatively flat and 9.3 km (D-F) where beds are severely tilted and faulted. The H components (X and R) are gained three times the amplitude of the Z component and all gathers have an outer mute of 45 degrees applied. Using the same parameterizations for KPSDM, the PP energy on all components is equally flattened (blue arrows) at both locations. Pink arrows on the 9.3 km CIGs highlight dipping bed reflections which are uniformly illuminated at all offsets on the Z component, but are illuminated differently between the positive and negative offsets of the X and R components.

266x288mm (300 x 300 DPI)

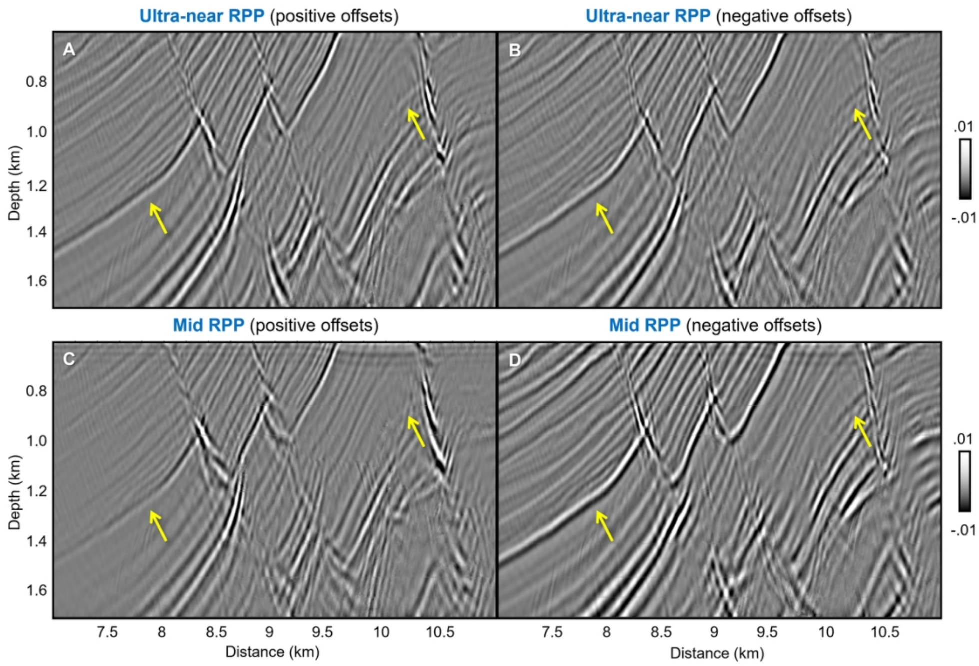

Figure 5: Comparison of the RPP ultra-near (upper row) and mid (lower row) partial-offset stacks for both positive (left column) and negative (right column) offsets. All panels are displayed on the same amplitude scale. Yellow arrows highlight left dipping bed reflections which are similarly imaged (disregarding polarity) on the ultra-near stacks but better imaged on the negative mid-offset stacks as a result of the biased HPP illumination to signed-offset.

163x111mm (300 x 300 DPI)

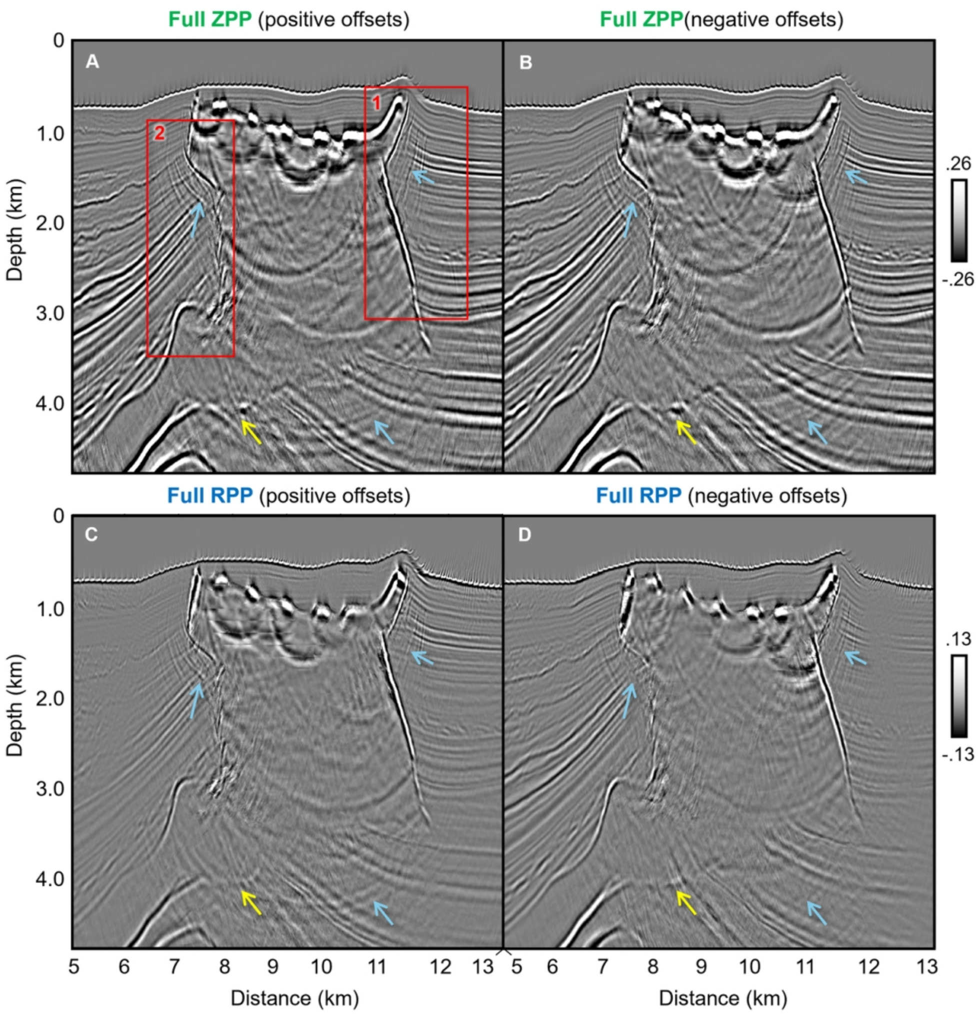

Figure 6: Comparison of full (0 to 45 degrees), signed-offset stacks for ZPP (upper panels) and RPP (lower panels) data. RPP images are gained two times the amplitude of the ZPP images. RPP illumination has a stronger SOI bias (compare the differences in panels C and D) versus the ZPP illumination (compare the minor differences in panels A and B). In general, RPP data supplement the ZPP data in critical locations below the salt overhangs and at the base of salt. Yellow arrows highlight the base of salt illumination which is more continuous on the RPP images as opposed to the ZPP images which are more affected by poorly migrated inter-salt multiples. Blue arrows highlight these multiples in regions below the salt and under the salt overhangs. Red boxes #1 and #2 on panel A outline the zoomed regions displayed in Figures 7 and 8 respectively.

123x130mm (300 x 300 DPI)

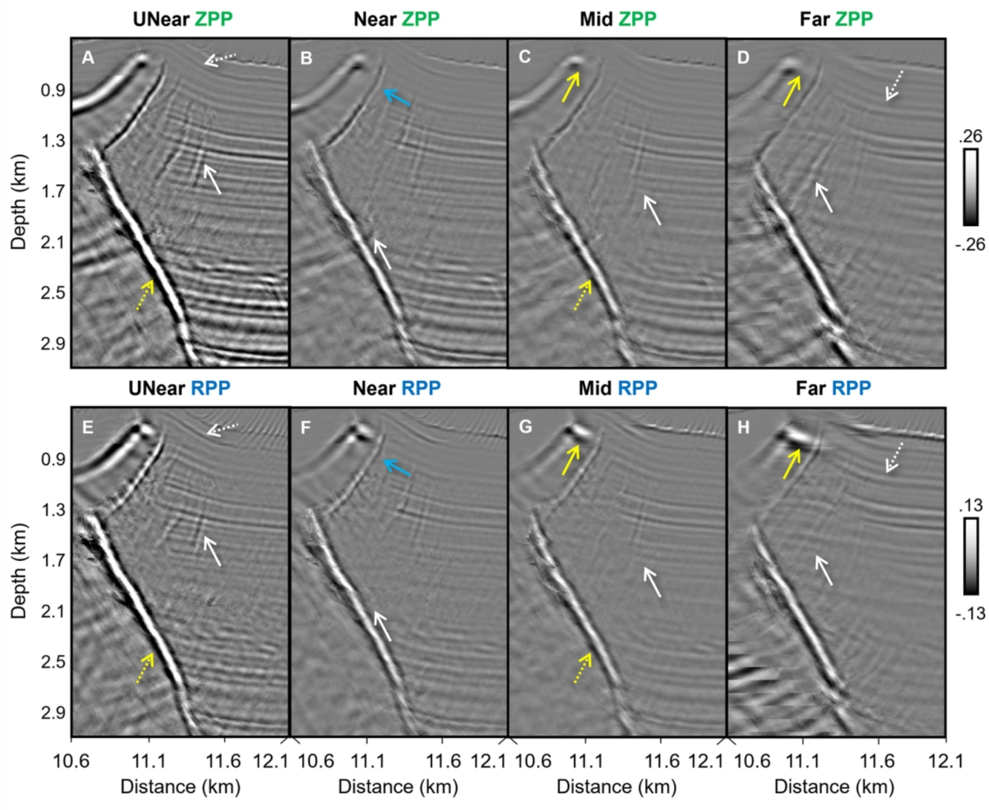

Figure 7: Positive partial-offset stacks zoomed to the right salt flank of the SEAM Phase 1 model. Zoomed region is described in Figure 6. Panels A-D show the ZPP ultra-near, near, mid, and far partial-offset stacks respectively and panels E-F show the RPP equivalent stacks. Generally, dotted arrows highlight reflectors that are comparably imaged on both Z and R components whereas solid arrows highlight examples where the RPP illumination is significantly better. Yellow arrows highlight observations related to salt imaging and white arrows highlight observations related to stratigraphy. Refer to the text for relevant details.

164x136mm (300 x 300 DPI)

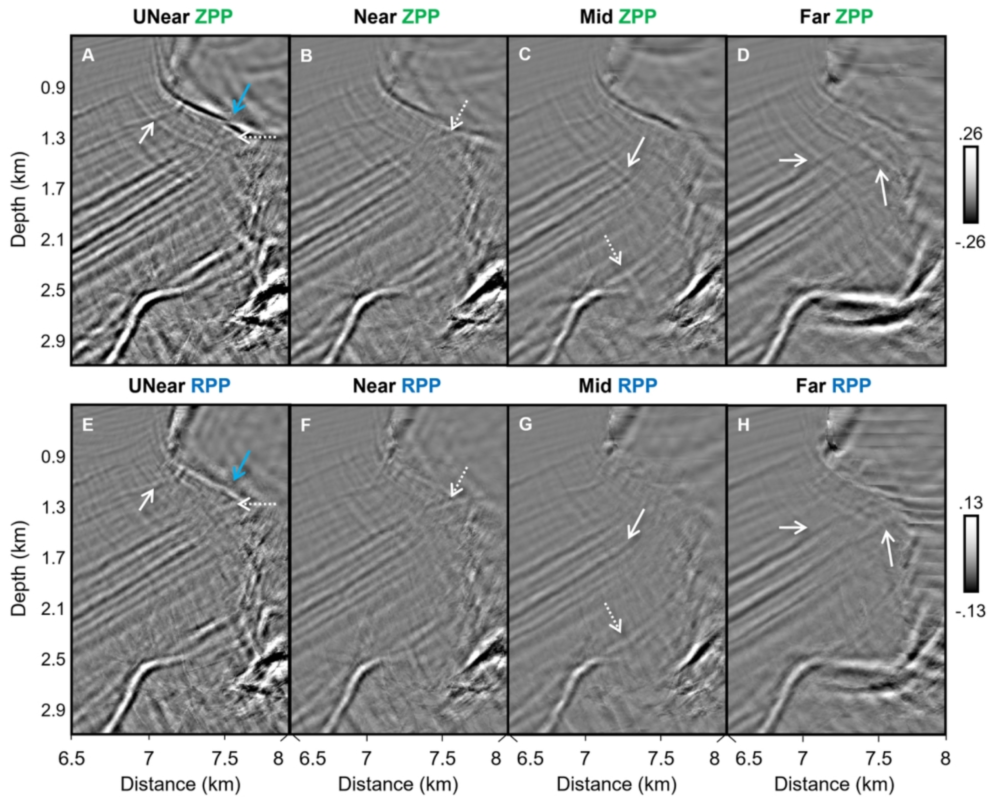

Figure 8: Negative partial-offset stacks zoomed to the left edge of the main salt body on the SEAM Phase 1 model. Zoomed region is described in Figure 6. Panels A-D show the ZPP ultra-near, near, mid, and far offset stacks respectively, and panels E-F show the RPP equivalent stacks. Descriptions of arrow annotations are the same as those used in Figure 7.

153x127mm (300 x 300 DPI)

DATA AND MATERIALS AVAILABILITY

Data associated with this research are available and can be obtained by#xD;#xA;contacting the corresponding author.

DOI:10.1190/int-2024-0145.1